Journal of Non-Newtonian Fluid Mechanics 242 (2017) 48–56

Contents lists available at ScienceDirect

Journal of Non-Newtonian Fluid Mechanics

journal homepage: www.elsevier.com/locate/jnnfm

Mean first passage time in a thermally fluctuating viscoelastic fluid

C. Hohenegger[a,*], R. Durr[a], D.M. Senter[a]

Department of Mathematics, University of Utah, 155 S 1400 E Room 233, Salt Lake City, UT 84112-0090, United States

ARTICLE INFO

Article history:
Received 10 June 2016
Revised 9 January 2017
Accepted 8 March 2017
Available online 9 March 2017

Keywords:
Viscoelastic fluid
Generalized Langevin equations
Anomalous diffusion
Mean first passage time

ABSTRACT

The motion of a passive spherical particle in a fluid has been widely described via a balance of force equations known as a Generalized Langevin Equation (GLE) where the covariance of the thermal force is related to the time memory function of the fluid. For viscous fluids, this relationship is simply a delta function in time, while for a viscoelastic fluid it depends on the constitutive equation of the fluid memory function. In this paper, we consider a general setting for linear viscoelasticity which includes both solvent and polymeric contributions, and a family of memory functions known as the generalized Rouse kernel. We present a statistically exact algorithm to generate paths which allows for arbitrary large time steps and which relies on the numerical evaluation of the covariance of the velocity process. As a consequence of the viscoelastic properties of the fluid, the particle exhibits subdiffusive behavior, which we verify as a function of the free parameters in the generalized Rouse kernel. We then numerically compute the mean first passage time of a passive particle through layers of different widths and establish that, for the generalized Rouse kernel, the mean first passage time grows quadratically with the layer's width independently of the free parameters. Along the way, we also find the linear scaling of the mean first passage time for a layer of fixed width as a function of the particle's radius.

1. Introduction

Many fundamental fluid processes arise through the interactions between suspended microstructures and a viscous background fluid. For example, mucus is a suspension of oligomeric mucin proteins in a water like fluid and whole blood is a suspension of red blood cells in plasma. Therefore, biological fluids have received a lot of attention recently, see for example [1–4]. When studying the macroscale characteristics of these systems, viscoelastic properties emerge [3,5], in other words such systems can display both elastic and viscous responses depending on the applied forces. One of the most widely used experimental technique to probe these viscoelastic liquids is passive microrheology, which records the fluctuations of a passive sphere and connects measurable quantities like mean square displacement to bulk mechanical properties, see [6–8] for details. The most recognizable signature of such viscoelastic liquids is that the mean square displacement of the particle's position scales sublinearly with time for a certain period of time before transitioning to pure diffusion. This subdiffusive behavior is usually refer to as anomalous diffusion to contrast with the diffusion of Brownian particles where the mean square displacement scales linearly with time. However, a quantity that remains poorly understood is the characterization of the mean first passage time or the average time it takes a particle to first traverse a layer of fluid. The classical theory of Brownian motion [9] predicts that, for a spherical particle undergoing thermal motion in a viscous fluid, the mean first passage time scales quadratically with the width of the layer. Recent progress has also been made in characterizing first passage in lattice models [10,11]. Finally, a few theoretical and numerical characterizations of the first passage time distribution for processes that exhibit anomalous diffusion and can be described by fractional Brownian motion or Lévy processes exist, see [4,12–14]. For example, Hill et al. [4] use experimental measurements in cultured mucus and a fractional Brownian motion model to predict the time it would take a particle to diffuse through a 25 μm thick mucus layer. While fractional Brownian motion, which is a Gaussian process, has been suggested as a better model than non-Gaussian continuous time random walk for a class of biological fluids, see [15,16], the recent work of Lysy et al. [17] shows that cultured mucus might be better described by a generalized Rouse kernel and Generalized Langevin Equation (GLE). Therefore, motivated by both the original question of Hill et al. [4] and the conclusion of Lysy et al. [17], we numerically study mean first passage time in a viscoelastic fluid that can be described by a GLE. Because of the choice of a generalized Rouse kernel to model the system's memory, the Gaussian particle's position process becomes non Markovian and non stationary.

* Corresponding author.
E-mail address: choheneg@math.utah.edu (C. Hohenegger).

http://dx.doi.org/10.1016/j.jnnfm.2017.03.001
0377-0257/

There is a long tradition of using GLEs to model thermal motion of a particle in a viscoelatic fluid with or without external forces [6–8,18–20]. However, none of these models consider the purely viscous solvent contribution to the motion. This assumption has lead to a singular behavior when taking the zero mass limit as observed by Indei et al. [21,22] and McKinley et al. [23]. Furthermore, the relative contribution of the solvent and of the suspended polymers is statistically unclear [24]. In order to be able to take the zero mass limit and to interpolate between viscous and viscoelastic diffusions, we consider both the solvent and the polymeric contributions, see also [25,26]. While Indei et al. [21] previously considered including the solvent viscosity (or inertia) in a three-parameter model of the dynamic modulus, their approach is not able to easily recover the classical Langevin equation for Brownian motion. Our GLE, which uses superposition to include both solvent and polymeric contributions independently in the deterministic and stochastic forces, does recover Brownian motion by setting a parameter to zero corresponding to the absence of polymers.

In the regime of linear viscoelasticity, where the stress tensor is best described by a Lodge integral equation [27], one of the most used three parameters family of memory relaxation kernel is the generalized Rouse kernel, an equally weighted sum of negatively decaying exponential kernels. Formally, for a number of kernels N, a relaxation time τ_0 and an exponent α, it is defined as

$$K(t) = \frac{1}{N}\sum_{n=0}^{N-1} e^{-|t|/\tau_n}, \tag{1}$$

where the discrete relaxation spectrum is chosen according to some phenomenological model. Here, we set

$$\tau_n = \tau_0\left(\frac{N}{N-n}\right)^{\alpha} \quad \alpha > 1 \quad n = 0,\dots,N-1. \tag{2}$$

In the above, α is the subdiffusive exponent, which is a function of the decay rate of the memory kernel and determines the slope of the subdiffusive phase [23]. On the other hand, N determines the length of the subdiffusive phase. Since cultured mucus shows subdiffusive behavior on all length scales [4,17], our ultimate goal is to consider the case when N becomes large.

The rest of this paper is organized as follows. In Section 2.1, we provide the details of the model describing the motion of the particle as well as the relevant definitions, while in Section 2.2, we develop a statistically exact algorithm which allows for the fast simulation of paths of arbitrary large but constant time steps. The algorithm relies on the numerical approximation of the covariance of the position process and is applicable to a larger set of parameters than the decomposition of the equation in a matrix of Ornstein-Uhlenbeck processes proposed by McKinley et al. [23]. In Section 2.3, we present a method for calculating the mean first passage time that accounts for paths which have not exited the layer at the end of the simulation time. In Section 3.1, we apply the algorithm to the characterization of the subdiffusive behavior and of the increment auto-correlation of the position's process for different set of free parameters. Finally, in Section 3.2, we establish the dependence of the mean first passage time on the width of the layer, of the particle's radius and of the number of kernels.

2. Method

2.1. Model

A spherical particle of mass m and radius r that diffuses freely in a viscoelastic environment is subject to both drag forces via viscous and elastic dissipation and diffusive forces via thermal fluctuations. The GLE for the one dimensional particle velocity $V(t)$ is then (see also [26])

$$m\frac{dV(t)}{dt} = -\gamma_s V(t) - \frac{\gamma_p}{\tau}\int_{-\infty}^{t} K(t-s)V(s)ds + \sqrt{\frac{k_B T\gamma_p}{\tau}}F(t) + \sqrt{2k_B T\gamma_s}\dot{W}(t). \tag{3}$$

The GLE (3) is a balance of forces equation that relates the particle's acceleration to its velocity history and to thermal fluctuations. Here k_B is the Boltzmann constant, T is the absolute temperature, $\gamma_s = 6\pi r\eta_s$ is the Stokes drag coefficient for a sphere in a fluid with solvent viscosity η_s, and $K(t)$ is a dimensionless memory kernel given by a constitutive law of viscoelasticity with viscosity $\eta_p = \eta_0 + \eta_s$ (η_0 is the zero shear rate viscosity) and polymeric time $\tau = \int_0^\infty K(t)dt$. The introduction of a polymeric time in (3) results from a dimensional argument since integrating the velocity history introduces an extra time unit. In (3), we also used the fact that the microscopic memory function is proportional to the bulk viscosity of the fluid with proportionality constant given by the drag coefficient [8,18]. Furthermore, we set $\gamma_p = 6\pi r\eta_p$. Because energy is stored in the elastic component of the fluid, the fluctuation-dissipation theorem applied to the zero mean Gaussian process $F(t)$ leads to the following form of its covariance [28]

$$\mathbb{E}[F(t)F(s)] = K(t-s). \tag{4}$$

Finally, $\dot{W}$ is a white noise in time with zero mean and covariance

$$\mathbb{E}[\dot{W}(t)\dot{W}(s)] = \delta(t-s). \tag{5}$$

For the generalized Rouse kernel in Eqs. (1) and (2), the polymeric time τ in (3) is simply the average relaxation time $\tau_{\text{avg}} = \frac{1}{N}\sum_{n=0}^{N-1}\tau_n$. Eq. (3) does not include contributions that might results from surface roughness or chemical interactions at the particle's surface.

In the language of continuum viscoelastic model, if $N = 1$ in (1), then the polymeric fluid stress in (3) satisfies the Oldroyd-B constitutive equation, see Appendix A for details. Further, we remark that the GLE (3) satisfies equipartition of energy [25,26], namely

$$\mathbb{E}[V(0)^2] = \frac{k_B T}{m}.$$

The form of (3) is different from the traditional form of [6,8] in that it includes both solvent and polymeric contributions to the fluid and that it reduces easily, by setting $\eta_p = 0$, to the classical Langevin equation of motion of a passive tracer in a viscous fluid.

Ultimately, we are interested in the position process $X(t)$ of the particle whose velocity satisfies the GLE (3). We formally define $X(t)$ as the pathwise integral

$$X(t) = \int_0^t V(s)ds \quad X(0) = 0. \tag{6}$$

To simplify notation in Eq. (3), we let $a = \gamma_s/m$, $b = \gamma_p/(\tau_{\text{avg}}m)$ and $c = \sqrt{k_B T/m}$, and we define $K^+(t) = K(t)u(t)$ where $u(t)$ is the unit step function. The GLE (3) with noise (4) and (5) becomes

$$\frac{dV(t)}{dt} = -aV(t) - b\int_{-\infty}^{\infty} K^+(t-s)V(s)ds + c\sqrt{b}F(t) + c\sqrt{2a}\dot{W}(t) \tag{7}$$

$$\mathbb{E}[F(t)F(s)] = K(t-s) \quad \mathbb{E}[\dot{W}(t)\dot{W}(s)] = \delta(t-s). \tag{8}$$

We note that the integral in (7) is simply the time convolution of $K^+(t)$ and $V(t)$. As is common practice, we make sense of the solution of (7) and (8) in Fourier space. We use the following definition of the Fourier transform, denoted by $\hat{\cdot}$:

$$\hat{f}(\omega) = \int_{-\infty}^{\infty} f(t)e^{-i\omega t}dt \quad f(t) = \int_{-\infty}^{\infty}\hat{f}(\omega)e^{i\omega t}d\omega.$$

A stochastic process $V(t)$ is a solution to (7) and (8) if its covariance is [28]

$$\widehat{\rho_V}(\omega) = \frac{c^2(2a + b\hat{K}(\omega))}{|i\omega + a + b\widehat{K^+}(\omega)|^2}. \tag{9}$$

Using the definition (1), the Fourier transform of the kernels in (9) are

$$\hat{K}(\omega) = \frac{1}{N}\sum_{n=0}^{N-1} \frac{2\lambda_n}{\lambda_n^2 + \omega^2} \quad \widehat{K^+}(\omega) = \frac{1}{N}\sum_{n=0}^{N-1} \frac{1}{\lambda_n + i\omega}.$$

where $\lambda_n = \tau_n^{-1}$, $n = 0, \ldots, N-1$ are the inverse of the relaxation times. We note that $V(t)$ is a non-Markovian stationary Gaussian process and that, because of the inertial term $i\omega$ and the two-sided Fourier transform in (9), there is no simple analytical expression for $\rho_V(t) = \mathbb{E}[V(t)V(0)]$.

Since $X(t)$ in (6) is a non Markovian, non stationary Gaussian process, it is uniquely determined by its covariance function, denoted by $\rho_X(t, s)$. Using (6), the definition of $\rho_X(t, s)$, and integration, we have

$$\rho_X(t, s) = \int_0^t \int_0^s \rho_V(|t' - s'|)ds'dt'. \tag{10}$$

For simplicity, we assume next that $t > s$. Breaking up the integral in (10) into two pieces and reversing the order of integration yields

$$\begin{aligned}\rho_X(t, s) = {} & tI_1(t) - (t - s)I_1(t - s) + sI_1(s) \\ & - [I_2(t) - I_2(t - s) + I_2(s)] \quad t > s.\end{aligned} \tag{11}$$

In Eq. (11),

$$I_1(t) = \int_0^t \rho_V(u)du \quad I_2 = \int_0^t u\rho_V(u)du$$

are the first and second moments of $\rho_V(t)$. Plugging $\rho_V(t)$ in terms of its inverse Fourier transform in $I_2(t)$ and using trigonometric identities, we find

$$I_2(t) = tI_1(t) - \frac{2}{\pi}\int_0^\infty \widehat{\rho_V}(\omega)\frac{\sin^2(\omega t/2)}{\omega^2}d\omega,$$

so that (11) simplifies to

$$\begin{aligned}\rho_X(t, s) &= J(t) + J(s) - J(t - s), \quad \text{where} \\ J(t) &= \frac{2}{\pi}\int_0^\infty \widehat{\rho_V}(\omega)\frac{\sin^2(\omega t/2)}{\omega^2}d\omega.\end{aligned} \tag{12}$$

Since the second term in the integrand of $J(t)$ is a rescaling of the sinc function and since $\widehat{\rho_V}(\omega)$ decays at infinity by construction (decay in memory of the system), the improper integral converges.

2.2. Algorithm

We now describe the algorithm necessary to generate paths realizations of $X(t)$ with covariance given by (12), assuming that $J(t)$ in (12) can be numerically evaluated. The technical details of the numerical integration of $J(t)$ are given in Appendix B. We describe the algorithm to create N_P discrete paths realizations of length N_T with time increment Δt whose discrete covariance matrix is given by $\mathbf{R}_{ij} = \rho_X(i\Delta t, j\Delta t)$, $i, j = 1, \ldots, N_T$. In general, $\mathbf{R}$ has full rank and is positive semi-definite. If, however, numerical errors lead to small negative eigenvalues of $\mathbf{R}$, then they are replaced by small positive eigenvalues and $\mathbf{R}$ is adjusted accordingly. The algorithm follows [29] and is summarized below.

1. Build $\mathbf{R}_{ij} = \rho_X(i\Delta t, j\Delta t)$, $i, j = 1, \ldots, N_T$, using (12);
2. Find the lower Cholesky decomposition of $\mathbf{R}$, such that $\mathbf{R} = \mathbf{C}\mathbf{C}^T$;
3. Pick $\mathbf{Y}$, a $N_T \times N_P$ matrix of $\mathcal{N}(0, 1)$ distributed random variables;
4. Set $\mathbf{X} = \mathbf{C}\mathbf{Y}$.

The columns of $\mathbf{X}$ are then single path realizations. The above algorithm is statistically exact and the only errors are deterministic due to the approximation of the integral in (12). We emphasis that for a fixed N_T, $\mathbf{C}$ only needs to be calculated once and steps 3 and 4 can just be repeated to increase the number of paths. However, the algorithm is not a forward marching scheme. In other words, to generate paths up to $N_{T'}$ with $N_{T'} > N_T$, the entire covariance matrix has to be calculated. For large N_T, steps 1 and 2 are the most computationally intensive. In particular, as the size of $\mathbf{R}$ increases, management of memory becomes important and we implement a block Cholesky decomposition.

Let $\mathbf{B}$ be a symmetric $N_T \times N_T$ matrix divided in blocks of size M. The number of rows of blocks is $k = M/N_T$ and the total number of Cholesky blocks is $1 + 2 + 3 + \ldots + k = \frac{k(k+1)}{2}$. Following the ideas of the construction of the Cholesky decomposition of a matrix, the general Cholesky blocks of $\mathbf{B}$ are

$$\mathbf{C}_{ii} = \text{Chol}(\mathbf{A}_{ii}) - \sum_{k=1}^{i-1} \mathbf{C}_{ik}\mathbf{C}_{ik}^T \quad i = 1, \ldots, k$$

$$\mathbf{C}_{ij} = \left(\mathbf{A}_{ij} - \sum_{k=1}^{j-1} \mathbf{C}_{ik}\mathbf{C}_{jk}^T\right)\mathbf{C}_{jj}^{-T} \quad i = 1, \ldots, k,\ j = 1, \ldots, i-1.$$

We use the structure of the block Cholesky decomposition of $\mathbf{R}$ to calculate the path $\mathbf{X}$ by writing $\mathbf{X}$ and the random normal vector $\mathbf{Y}$ in block form as well. Let $\mathbf{X}_i$, $\mathbf{Y}_i$, $i = 1, \ldots, k$ denote the block vectors of length M of $\mathbf{X}$ and $\mathbf{Y}$. Then, the path realization in block form becomes

$$\mathbf{X}_i = \sum_{j=1}^{i} \mathbf{L}_{ij}\mathbf{Y}_j \quad i = 1, \ldots, k.$$

2.3. Mean first passage time calculation

The mean first passage time (MFPT) is the average time that it takes a particle to first exit a layer of width w. In other words, only the first time that the particle reaches w is recorded and ulterior positions are discarded. For simplicity, we set $X(0) = 0$ and record the first time T^1_{exit} such that $|X(T^1_{\text{exit}})| > w$. Physically, this set-up corresponds to a particle starting in the middle of a layer of width $2w$ and exiting through the top or bottom boundary. The MFPT is then taken to be the sample mean of T^1_{exit} over N_P paths. In order to obtain accurate statistics, we need to properly account for survivor paths. We call a path a survivor at T_{final}, if $|X(T_{\text{final}})| < w$. If there are too many survivor paths, then setting $T^1_{\text{exit}} = T_{\text{final}}$ for survivor paths would skew the distribution of first passage times and give the wrong MFPT. If the simulation could be run to a very large time, then there should be no survivor paths. This method is however computationally unrealistic. Instead, we develop a two steps approach to both minimize the number of survivor paths and adjust the MFPT accordingly.

First, we increase $T_{\text{final}} = N_T\Delta t$ so that the relative number of survivor paths is smaller than κ, where $0 < \kappa < 1$ is a threshold value. In other words, up to a relatively small number of paths, all paths have exited the layer before T_{final}. Since the algorithm uses the entire time history (see Section 2.2), increasing T_{final} leads to generating new covariance matrices of size $N_T \times N_T$. Therefore, simply increasing N_T and keeping Δt fixed becomes unmanageable in terms of the memory needed to store the covariance matrices and find their Cholesky decompositions. Thus, we instead increase Δt to $(1 + \beta)\Delta t$ with $\beta > 0$, and we set $N_T = 2^{13}$. We then generate new paths, compute the relative number of survivors

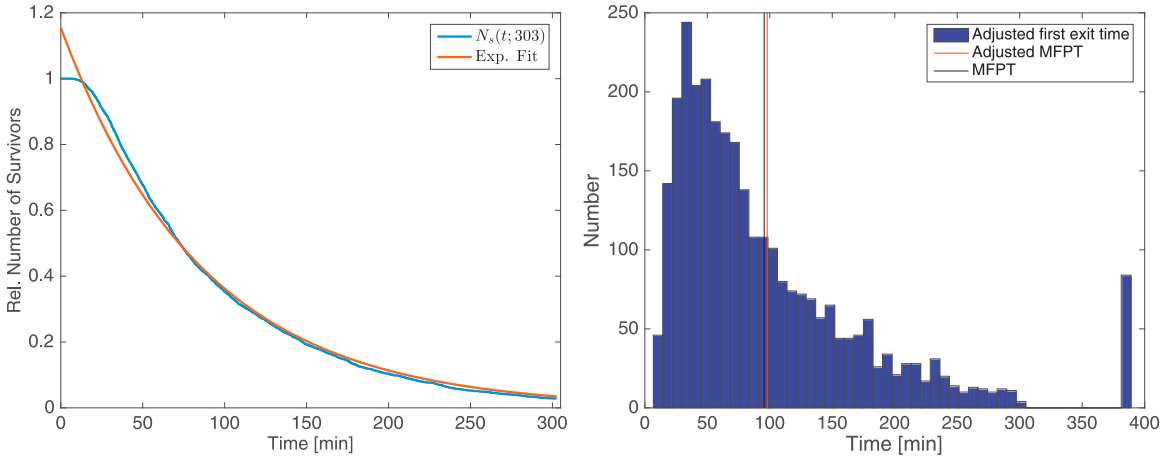

(a) $N_S(t;303)$. (b) Exit times.

Fig. 1. (a) Relative number of survivors, $N_S(t;T^*_{\text{final},w})$, as a function of time t for $N=16$, $w=r=1$ μm, $\alpha=2$. $T^*_{\text{final},w}=303$ min is chosen so that 98% of the paths have exited, all other parameters are given in Table 1. The orange line is the exponential fit of the tail. (b) Histogram of the adjusted first passage time together with adjusted MFPT (red) and non-adjusted MFPT (black) for the same parameters as (a). (For interpretation of the references to color in this figure legend, the reader is referred to the web version of this article.)

Table 1
List of physical parameters.

Parameter	Symbol	Values	Units
Tracer density	ρ	1.05 and 105	1×10^{-2} mg μm^{-3}
Tracer radius	r	0.5, 1 and 2	μm
Sol. viscosity	η_s	1	1×10^{-6} MPa ms
a parameter	$a=\frac{\gamma_s}{m}$	1.7, 0.4 and 0.1	1×10^{4} ms^{-1}
b parameter	$b=\frac{\gamma_p}{\tau_{\text{avg}}m}$	1.7, 0.4 and 0.1	1×10^{6} ms^{-1}
Boltz. x temp.	k_BT	4.1	1×10^{-2} μm^2 mg ms^{-2}
c parameter	$c=\sqrt{\frac{k_BT}{m}}$	2.7, 1 and 0.3	μm^2 ms^{-2}
Pol. viscosity	$\eta_p=100\eta_s$	1	1×10^{-4} MPa ms
First relax. time	τ_0	1	ms
Rouse exponent	α	2 and 4	

and repeat the process until T_{final} is large enough to guarantee that $(1-\kappa)100\%$ of the paths have exited the layer. We denote by $T^*_{\text{final},w}$ the final simulation time found that satisfies the previous condition and use the subscript w to emphasize the dependence on the layer's width w.

Second, we adjust the values of the exit times for the survivor paths. In order to do so, we calculate the relative number of survivor as a function of time, which is defined as

$$N_S(t;T^*_{\text{final},w}) = \frac{\#\{X(s),0\le s\le T^*_{\text{final},w} : T^1_{\text{exit}}>t \text{ and } |X(T^1_{\text{exit}})|>w\}}{N_P}.$$

In the above, # denotes the number of elements in the set. For illustrative purposes, we plot in blue, in Fig. 1(a), $N_S(t;T^*_{\text{final},w})$ for $N=16$, $\alpha=2$, $w=1$ μm and $r=1$ μm and parameters given below in Table 1. In this case, $T^*_{\text{final},w}=303$ min so that 98% of the paths have exited. We observe that, for all tested choices of α, N, w, r, the tail of $N_S(t;T^*_{\text{final},w})$ is exponential, as shown in Fig. 1(a). Therefore, it can be fitted by an exponential curve of the form $p(t)=a_1\exp(-a_2t)$ for t sufficiently large. The exponential fit is plotted as an orange line in Fig. 1(a). This is equivalent to saying that for t large the probability density of the first passage time is $p(t)$. The mean first passage time conditioned on the fact that the path survives can now be estimated from the definition of the conditional expectation and $p(t)$. The details of this calculation are given in Appendix C. We find that the adjusted exit time for survivor paths is $T^1_{\text{exit}}=T^*_{\text{final},w}+1/a_2$. Fig. 1(b) shows the histogram of the adjusted first passage time with the same parameters as in Fig. 1(a). The vertical red line represents the adjusted MFPT (98 min), while the black line represents the MFPT (95 min) if the first passage time for survivor paths is taken as $T^*_{\text{final},w}$. In what follows, we will simply refer to the adjusted MFPT as the MFPT.

3. Results and discussion

We choose ms as the unit of time, μm as the unit of length and mg as the unit of mass. With these definitions the unit of force is μN, while the unit of stress is MPa. For the generalized Rouse kernel in Eqs. (1) and (2), the viscosity η_p is related to the modulus G_0 by $\eta_p=G_0\tau_{\text{avg}}$ [27]. At this point, we are faced with the choice of fixing either the viscosity η_p or the modulus G_0. Since fixing G_0 corresponds to a constant coefficient in the continuum fluid-stress model [26], we set $G_0=1\times10^{-4}$ mg/ms^2, which is comparable to the value of Indei et al. [21] for a single mode relaxation liquid. In particular, for $N=1$, we have $\eta_p=100\eta_s$, where we take η_s to be the viscosity of water. We compute the mass of the particle as $m=4/3\pi r^3\rho$, where ρ is either the density of polystyrene beads (comparable to that of water) or a hundred times denser than water. Recalling the definitions of Section 2.1, we have $a=\gamma_s/m=9\eta_s/(2\rho r^2)$ and $b=\gamma_p/(\tau_{\text{avg}}m)=9G_0/(2\rho r^2)$. Table 1 summarizes the relevant parameters.

3.1. Mean square displacement and increment auto-correlation

As a first check, we verify that the particle ensemble mean square displacement (MSD) defined as $M(t)=\langle X(t)^2\rangle$, where $\langle\cdot\rangle$ is the sample mean over $N_P=3\times10^3$ paths realizations, exhibit subdiffusive behavior. Indeed, in Fig. 2, we plot the MSD for a particle of radius $r=1$ μm for $\alpha=2$ and $N=1$, 5, 20 and 40 in (a) and for $\alpha=2$ and 4 and $N=1$ and 40 in (b). If $N=1$, it has been previously argued [30] that the MSD grows linearly as in the viscous case, which is the case for the blue line in Fig. 2(a) and for the indistinguishable blue and orange lines in Fig. 2(b). Because the covariance based algorithm is statistically exact, we can choose relatively large time steps and explore the transition from subdiffusive to diffusive behavior. To obtain Fig. 2, we set $\Delta t=2$ ms and $N_T=2^{13}$, corresponding to a maximum time of a little more than 10 s. We observe two further expected facts, namely that as N increases, the MSD becomes subdiffusive with slope $1/\alpha$ (dashed lines in Fig. 2) and the subdiffusive phase lasts longer [23]. Increasing N from 5 to 40 results in a growth of the subdiffusive phase

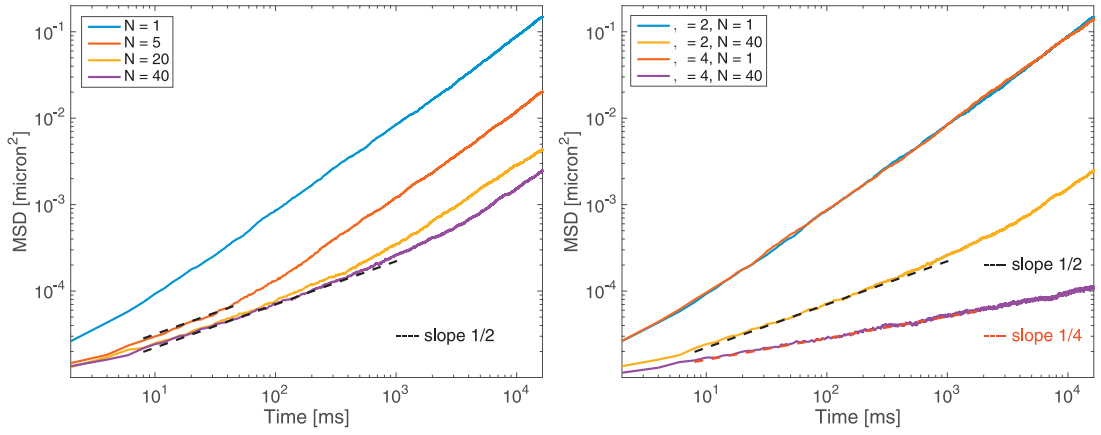

(a) Role of N. (b) Role of α.

Fig. 2. Particle MSD as a function of time on a log-log scale for $N = 1$, 5, 20 and 40 and $\alpha = 2$ in (a) and for $\alpha = 2$ and 4 and $N = 1$ and 40 in (b). The parameters are given in Table 1 with $r = 1$ μm. In (a), both dashed lines have slope 1/2, while in (b), the dashed lines have slope 1/2 (black) and 1/4 (red) respectively. (For interpretation of the references to color in this figure legend, the reader is referred to the web version of this article.)

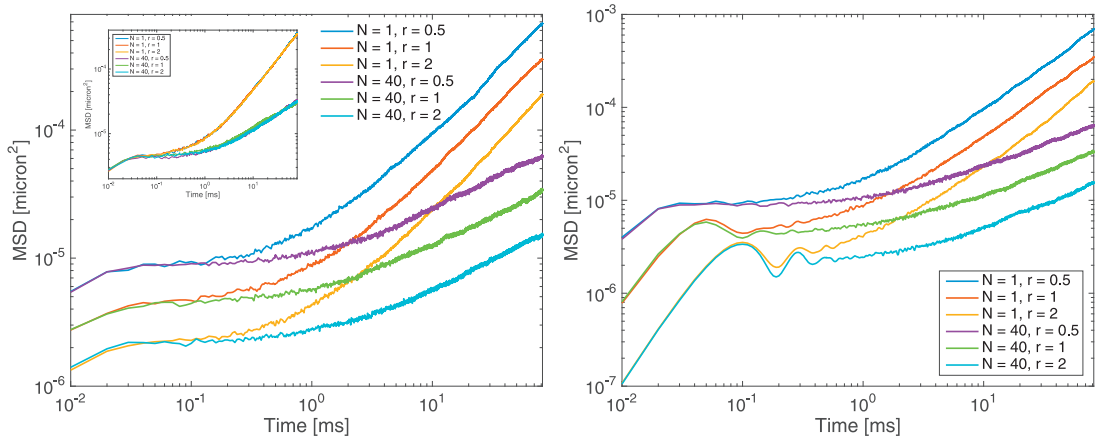

(a) $\rho = 1.05 \times 10^{-9}\,\mathrm{mg\,\mu m^{-3}}$. (b) $\rho = 1.05 \times 10^{-7}\,\mathrm{mg\,\mu m^{-3}}$.

Fig. 3. Particle MSD as a function of time on a log-log scale for $N = 1$ and 40 and $r = 0.5$ μm 1 μm and 2 μm for a neutrally buoyant particle in (a) and for a hundred times denser particle in (b). The parameters are given in Table 1 with $\alpha = 2$. The inset in (a) shows the rescaling of the MSD with the inverse of the radius.

from 0.05 s to 3 s (black dashed lines in Fig. 2(a)). Furthermore, we see in Fig. 2(b) that the length of the subdiffusive phase also depends on α. Indeed, for $\alpha = 2$ the transition to pure diffusion (black dashed line) happens about 1 s earlier than for $\alpha = 4$ (red dashed line).

Next, in Fig. 3, we focus on the role of the mass for $\alpha = 2$ and the small time regime, where we set $\Delta t = 0.01$ ms and $N_T = 2^{13}$. In Fig. 3(a), we consider a neutrally buoyant particle with $\rho = 1.05 \times 10^9$ mg/μm^{-3} and in Fig. 3(b) a hundred times denser particle. We note that the inertia of the particle leads to the oscillatory behavior of the MSD at short times [21,23], but its influence is only significant for a particle a hundred times denser than water and at frame rates currently unattainable experimentally. In this case, other effects like sedimentation might be important and might need to be considered in the balance of forces equation. At time scales longer than the first relaxation time $\tau_0 = 1$ ms, we see similar behaviors for both set of particles and radii with the heavier and larger particle diffusing more slowly than the lighter and smaller particle. In writing down Eq. (3), we used the fact that the drag coefficient was proportional to the radius of the particle, which for either the viscous case or the polymeric case translates into a diffusion coefficient that is inversely proportional to the radius [6,18]. We verify numerically that this observation extends to the GLE (3) in the inset of Fig. 3(a), where we rescaled the MSD by the radius for both $N = 1$ and 40.

Another useful empirical statistical measure to compare to experimental data is the ensemble increment auto-correlation function (ACF) of the particle's position process. In Fig. 4, we plot the increment ACF for $N = 1$, 5, 20 and 40 and $\alpha = 2$ and 4 for a particle with $\rho = 1.05 \times 10^9$ mg/μ^{-3} in 4(a) and for a hundred times denser particle in 4(b). The lag times are multiples of $\Delta t = \tau_0 = 1$ ms, the smallest relaxation time. As in experimental data [4,17], we show first lag anti-correlation in the increment ACF. However contrary to experimental data, the length of the anti-correlation is independent of the subdiffusive exponent α. This behavior was also observed in numerical simulations of a fluid-particle system [26]. As opposed to the MSD data, the density of the particle plays no role in the increment ACF and the exact same increment ACF plots are observed in Fig. 4(a) and (b). This fact suggest, as first discussed in [17], that the increment ACF produces a less noisy and more robust statistical measurement and should be combined with MSD data to extract the fluid's viscoelastic properties.

3.2. Mean first passage time

In the section, we only consider a particle with $\rho = 1.05 \times 10^9$ mg/μm^3. Following a numerical exploration of the different

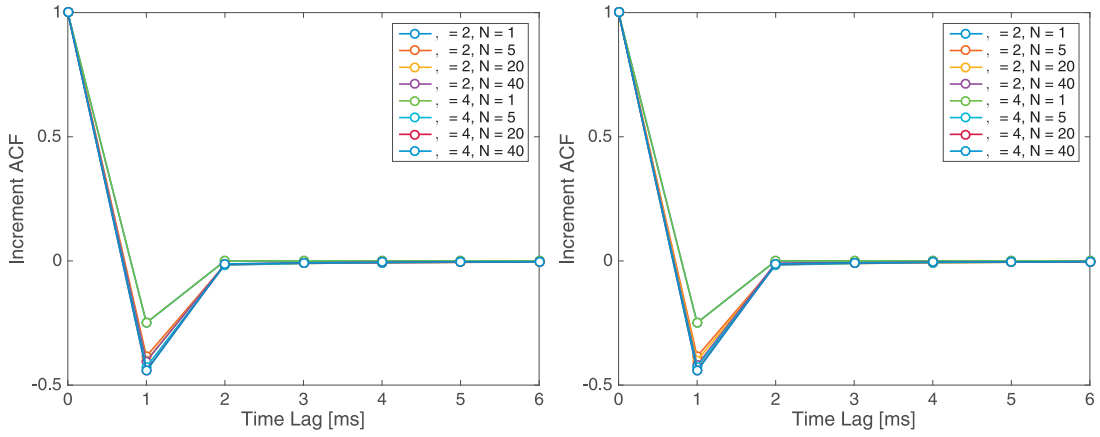

(a) $\rho = 1.05 \times 10^{-9}\,\mathrm{mg\,\mu m^{-3}}$. (b) $\rho = 1.05 \times 10^{-7}\,\mathrm{mg\,\mu m^{-3}}$.

Fig. 4. Particle increment ACF as a function of lag time for $N = 1$, 5, 20 and 40 and $\alpha = 2$ and 4 for a neutrally buoyant particle in (a) and for a hundred times denser particle in (b). The parameters are given in Table 1 with $r = 1$ μm.

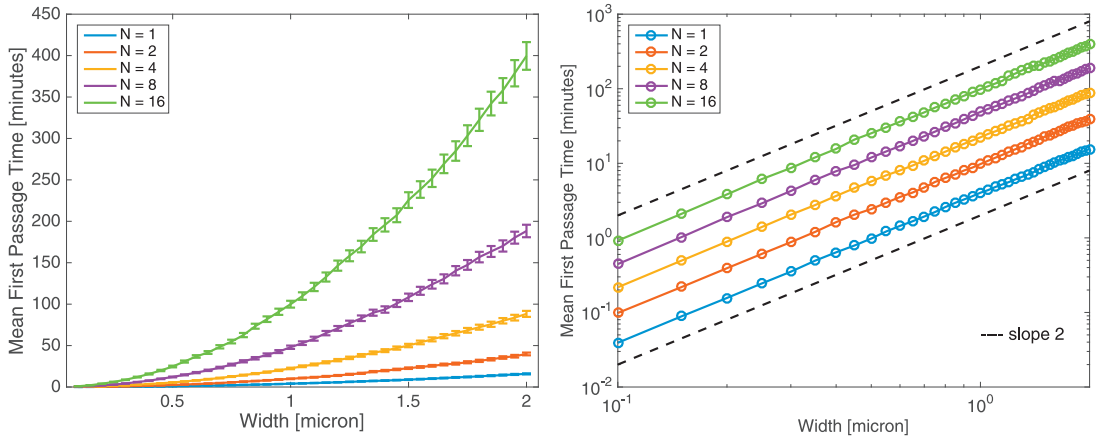

(a) 95% confidence interval. (b) Log-log plot.

Fig. 5. Mean first passage time in minutes as a function of the layer width $w \in [0.1, 2]$ μm with 95% confidence interval in (a) and on a log-log scale in (b) for $N = 1$, 2, 4, 8 and 16 and $\alpha = 2$. The parameters are given in Table 1 with $r = 1$ μm. In (b), the dashed lines have slope 2 and the stars are values of the linear fit.

values, we find that using large values of κ leads to a relative error of 6–9%, while larger values of β or N_P give relative errors of 1–3%. As a result, we choose $N_P = 3 \times 10^3$, $\beta = 0.5$, and $\kappa = 0.02$, corresponding to less than 2% survivor paths at T_{final}. In Fig. 5, we plot the MFPT as a function of w, for $w \in [0.1, 2]$ μm and $N = 1$, 2, 4, 8 and 16. To account for the uncertainties in the estimation of the MFPT discussed in Section 2.3, we include error bars in Fig. 5. Since the standard deviation of the first passage time is unknown, the length of the error bar is calculated as $t^* s/\sqrt{N_P}$ where $t^* = 2.8$ is the upper 0.025 critical value for the t distribution with $N_P - 1$ degrees of freedom and s is the sample standard deviation. This choice of t^* corresponds to a 95% confidence interval. We note that the y axis has been rescaled to minutes, so that it takes a particle with $r = 1$ μm about one hour to diffusive through a layer twice its width if $N = 16$, while it only takes about 10 min if $N = 1$ (Fig. 5(a)). For comparison, the subdiffusive phase (see Fig. 2) lasts about one second if $N = 16$. With the above parameters, it would take about 12 h if $N = 16$ and 2 h if $N = 1$ for a 1 μm particle to diffuse through a 25 μm mucus layer. The discrepancy between the above prediction and the results of Hill et al. [4] can be explained by the fact that we do not have a good estimate for η_p for cultured mucus.

When plotted on a log-log scale in Fig. 5(b), we observe that the MFPT scales quadratically (the dashed lines have slope 2) with w, independently of the choice of N. This same results holds for $\alpha = 4$, with the only difference being that the MFPTs are about twenty times bigger. We recall that the same scaling law was obtained for Brownian motion [9]. We further confirm this intuition by fitting the natural logarithm of MFPT as a function of the logarithm of the width with a polynomial of degree one of the form $p_1 \ln(w) + p_2$. For all values tested, $p_1 \approx 2$. Thus, we claim

$$\mathrm{MFPT}(w) = C_1(N, \alpha) w^2 \quad \text{if} \quad r = 1\mu\mathrm{m}, \tag{13}$$

where we used the notation $C_1(N, \alpha) = \exp(p_2)$ to emphasize the dependence on the free parameters. Table 2 lists the values of $C_1(N, \alpha)$ and of the root mean square error of the linear fit of the logarithm for $N = 1$, 2, 4, 8 and 16 and $\alpha = 2$ and 4. From the C_1 column in Table 2, we notice that, for $\alpha = 2$, the ratio between subse-

Table 2
Values of the leading coefficient of the quadratic polynomial fit of the MFPT and root mean square error of the fit.

(N, α)	$C_1 = \exp(p_2)$	RMSE	(N, α)	$C_1 = \exp(p_2)$	RMSE
(1, 2)	3.97	0.015	(1, 4)	3.95	0.016
(2, 2)	9.8	0.017	(2, 4)	33.4	0.016
(4, 2)	22.2	0.012	(4, 4)	269.5	0.019
(8, 2)	47.8	0.017	(8, 4)	2.166d3	0.02
(16, 2)	98.7	0.017	(16, 4)	1.736d3	0.017

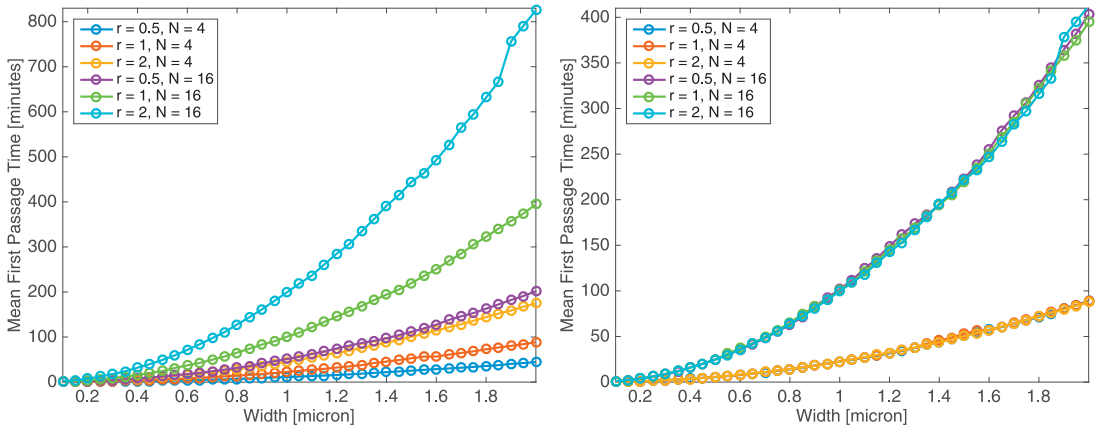

Fig. 6. Mean first passage time in minutes as a function of the layer width $w \in [0.1, 2]$ μm for $r = 1$ μm, 0.5 μm, and 2 μm, $N = 4$ and 16 in (a) and rescaled by the inverse of the radius in (b). The parameters are given in Table 1 with $\alpha = 2$.

quent C_1-values is about 2, while it is about 8 for $\alpha = 4$. This fact is further confirmed by Fig. 5(b), where each line is about $\ln(2)$ away from the line immediately below it. Since N was increased by a factor of 2, we have $C_1(2^k, \alpha) = 2^{\alpha-1} C_1(2^{k-1}, \alpha)$ and the proposed relationship for the MFPT (13) becomes

$$\mathrm{MFPT}(w) = N^{\alpha-1} C_1(1, \alpha) w^2 \quad \text{if} \quad r = 1\mu\mathrm{m}. \tag{14}$$

Finally, we explore the dependence of the MFPT and of $C_1(1, \alpha)$ on the particle's radius. In Fig. 6(a), we plot the MFPT for $r = 1$ μm, 05 μm, and 2 μm, $N = 4$ and 16, and $\alpha = 2$. For each N, the collapse of the data in Fig. 6(b) is obtained by multiplying the MFPT by the inverse of the radius. In other words, the MFPT scales linearly with the radius, independently of α.

In summary, we propose the following scaling of the MFPT as a function of the number of kernel N, the radius r and the layer's width w

$$MFPT(w, r) = C N^{\alpha-1} r w^2. \tag{15}$$

The constant C, obtained for $N = 1$, depends on the physical parameters of the viscoelastic constitutive equation (η_s, G_0, τ_0, α) of the generalized Rouse kernel in Eqs. (1) and (2).

3.3. Conclusion

In this paper, we presented a covariance based algorithm for the realizations of paths for a particle which obeys a Generalized Langevin Equation that includes both solvent and polymeric contributions. The algorithm only relies on the Gaussian structure of the processes and it is used to generate paths with arbitrary large time steps and for a wide range of physical parameters described by a generalized Rouse kernel. Using simulated data, we demonstrated that the mean square displacement is subdiffusive with slope inversely proportional to the exponent in the Rouse kernel and that the increment auto-correlation shows first lag anti-correlation. Finally, we established that the mean first passage time of simulated paths grows quadratically with the width of the layer and linearly with the radius of the particle. Both in the generation of the paths and in the estimation of the mean first passage time careful attention was paid to the underlying stochastic processes to guarantee statistical accuracy.

Understanding the role inertia plays in passive microrheology remains an open challenge [21,23]. While we were able to establish the traditional signature of inertia at small time scales in the mean square displacement, we only achieved this for particles that are a hundred times denser than water. For such heavy particles, the one dimensional balance of forces considered here might not be valid anymore. On the other hand, we pointed out that the increment auto-correlation function is independent of the mass, which suggests that it might serve as a better statistical estimator for the mechanical characteristics of the fluid. However, we are not aware of any protocol that connects the increment auto-correlation to the loss and storage moduli in a simple way as the one point microrheology of [6] does.

Our results have been presented for one dimensional motion, since the diffusion's coefficient of a sphere is the same in all directions. However, if ellipsoids or rods that have different diffusion coefficients were considered, then the GLE (3) can be vectorized and generalized to three dimensional motion and potentially used to probe anisotropic diffusion, see also [31].

In this paper, we presented the first exploration and characterization of the mean first passage time of a particle described by a Generalized Langevin Equation. Nevertheless, much work remains to be done both on the theoretical and experimental sizes to validate the above predictions and to better understand the distributions of first passage times and of hitting probabilities.

Acknowledgments

C. H. thanks D. Khoshnevisan, F. Rassoul-Agha and S. A. McKinley for useful discussions. R. D. and D. M. S. were partially supported through the research for undergraduate opportunities (REUs) from the Mathematics department at Utah. C. H. and D. M. S were partially supported by grant NSF-DMS 1413378.

Appendix A. Relationship to continuum models

In this appendix and in [26], we show the relationship between the form of the memory kernel and continuum model of extra stress. Following Larson [27], the deterministic stress tensor can be decomposed into a solvent contribution $\mathbf{\Sigma}_{\mathrm{det,s}}$ and a polymeric contribution $\mathbf{\Sigma}_{\mathrm{det,p}}$. The solvent stress is the Newtonian stress tensor

$$\mathbf{\Sigma}_{\mathrm{det,s}} = -p\mathbf{I} + 2\eta_s \mathbf{E}, \tag{A.1}$$

where p is the pressure, $\mathbf{I}$ is the identity matrix, $\mathbf{E} = (\nabla\mathbf{u} + \nabla\mathbf{u}^T)/2$ is the rate-of-strain tensor, and η_s is the solvent dynamic viscosity. As in [8,18,27], we consider the small strain limit for the polymeric stress tensor resulting in a linear viscoelastic model. In this setting, the constitutive equation for $\mathbf{\Sigma}_{\mathrm{det,p}}$ is known as the Lodge equation

and it has the form

$$\mathbf{\Sigma}_{\text{det,p}} = G_{\text{avg}}\mathbf{I} + 2\int_{-\infty}^{t} G_{(r)}(t-t')\mathbf{E}(t')\mathrm{d}t', \tag{A.2}$$

where G_{avg} is the modulus and $G_{(r)}(t)$ is the relaxation modulus (units of [stress]). The response is causal in the sense that $G_{(r)}(t) = 0$ for $t < 0$. Combining (A.1) and (A.2), we have

$$\mathbf{\Sigma}_{\text{det}} = -(p - G_{\text{avg}})\mathbf{I} + 2\eta_s\mathbf{E} + 2\int_{-\infty}^{t} G_{(r)}(t-t')\mathbf{E}(t')\mathrm{d}t'. \tag{A.3}$$

The zero shear-rate viscosity η_0 is related to $G_{(r)}(t)$ by $\eta_0 = \eta_s + \int_0^\infty G_{(r)}(t')\mathrm{d}t'$. If $G_{(r)}(t)$ is a single mode Maxwell model, $G_{(r)} = \frac{\eta_p}{\tau}e^{-t/\tau}$, where τ is the relaxation time and η_p is the polymeric dynamic viscosity related to G_{avg} by $\eta_p = G_{\text{avg}}\tau$ [27], then $\boldsymbol{\sigma}_{\text{set}} = \mathbf{\Sigma}_{\text{det}} + (p - G_{\text{avg}})\mathbf{I}$ satisfies the Oldroyd-B equation

$$\tau\overset{\triangledown}{\boldsymbol{\sigma}}_{\text{det}} + \boldsymbol{\sigma}_{\text{det}} = 2\eta_0\left(\mathbf{E} + \frac{\tau\eta_s}{\eta_0}\overset{\triangledown}{\mathbf{E}}\right),$$

where $\eta_0 = \eta_s + \eta_p$, and $\overset{\triangledown}{\cdot}$ is the upper convected time derivative defined as $\overset{\triangledown}{\mathbf{S}} = \frac{d\mathbf{S}}{dt} - \nabla\mathbf{u}^T\mathbf{S} - \mathbf{S}\nabla\mathbf{u}$. If the solvent viscosity is negligible, $\eta_s = 0$, then $\boldsymbol{\sigma}_{\text{det}}$ satisfies the Upper Convected Maxwell equation

$$\tau\overset{\triangledown}{\boldsymbol{\sigma}}_{\text{det}} + \boldsymbol{\sigma}_{\text{det}} = 2\eta_p\mathbf{E}.$$

Appendix B. Calculation of $J(t)$

We present a numerical method for the evaluation of $J(t)$ in (12), which relies on residue calculus as opposed to a quadrature scheme. We let $\gamma = b/N$, $\lambda_j = \tau_j^{-1}$, $j = 0, \dots, N-1$ and we define the polynomials

$$p(x) = \prod_{j=0}^{N-1}(x + \lambda_j) \quad q(x) = (x+a)p(x) + \gamma p'(x),$$

where $'$ denotes the derivative of $p(x)$ with respect to x. From these definitions and (9), it is easy to see that

$$\widehat{\rho_V}(\omega) = c^2\left[\frac{p(i\omega)}{q(i\omega)} + \frac{p(-i\omega)}{q(-i\omega)}\right] := c^2\Psi(\omega).$$

Since the roots of $p(x)$ are $-\lambda_{N-1} < \ldots < -\lambda_0 < 0$, $q(x)$ has $N-1$ roots located between the extrema of $p(x)$. For practical applications, we assume that either $-a < -\lambda_{N-1}$ or $-a > -\lambda_0$. In the first case, $q(x)$ has an extrema between $-\lambda_{N-1}$ and $-a$ and depending on the magnitude of γ, the last pair of roots is either a complex conjugate pair with negative real part or two purely real negative roots. In the latter case, $q(x)$ has an extrema between $-a$ and $-\lambda_0$ and the same conclusions can be reached about the location of the last two roots. We denote by $\omega_0, \dots, \omega_N$ the $N+1$ roots of $q(i\omega)$ in the upper half plane with $\omega_0, \dots, \omega_{N-2} \in i\mathbb{R}^+$, $\text{Im}(\omega_{N-1}$ and $\omega_N) \in \mathbb{R}^+$ with $\text{Re}(\omega_{N-1}) = -\text{Re}(\omega_N)$ or $\text{Re}(\omega_{N-1}) = \text{Re}(\omega_N) = 0$. Here, $\text{Im}(z)$ denotes the imaginary part of z, while $\text{Re}(z)$ is the real part of z. The roots of $q(-i\omega)$ are the complex conjugates of $\omega_0, \dots, \omega_N$. Since $a \neq \lambda_j$, $j = 0, \dots, N-1$, the poles of $\Psi(\omega)$ are simple. In [25], we derived an integral formula for integrals of the type $\int_0^\infty G(\omega)\text{sinc}^a(x)dx$, where a is even, sinc is the sinc function, and $G(\omega)$ has simple poles, appropriate decay and no real poles. The formula is a result of careful integration and the residue theorem. Letting $a = 2$, $G(\omega) = \Psi(\omega)$, and changing variables from ω to $\tilde{\omega} = \omega t/2$ yield [25]

$$J(t) = c^2\left[\frac{t}{2}\Psi(0) + \sum_{n=0}^{N}\text{Im}\left[\text{Res}(\Psi, \omega_n)\frac{e^{it\omega_n} - 1}{\omega_n^2}\right]\right]. \tag{B.1}$$

In the above, $\text{Res}(\Psi, \omega_n)$ denotes the residue of Ψ evaluated at ω_n, $n = 0, \dots, N$.

If the poles were analytically known, then (B.1) would be exact. However, there is no simple analytical formula for the poles if $N \geq 2$. Therefore, using (B.1) to evaluate $J(t)$, we have replaced an improper integration problem with a root finding problem. While this poses a restriction on how big N can be, Eq. (B.1) is numerically advantageous over an adaptive integration scheme of (12) for two reasons. First, the roots and residues can be precomputed and t only needs to be plugged into the right-hand side of (B.1). Second, because of the sinc function, the integrand is highly oscillatory and many subintervals are required to guarantee accuracy of a quadrature scheme.

To compute the residues, we first expand $p(i\omega)$ and $q(i\omega)$ into their series expansion using Vieta's formula. We have

$$p(i\omega) = i^N\sum_{j=0}^{N}(-1)^j\omega^{N-j}t_j \quad q(i\omega) = i^{N+1}\sum_{j=0}^{N+1}(-1)^j s_j\omega^{N+1-j}. \tag{B.2}$$

Here $t_0, \dots, t_N$ are the elementary symmetrical polynomials of $i\lambda_j$, $j = 0, \dots, N$, in other words

$$t_0 = 1 \quad t_1 = i\sum_{j=0}^{N-1}\lambda_j \quad t_2 = -\sum_{0=j_1}^{N-1}\sum_{j_2=j_1+1}^{N-1}\lambda_{j_1}\lambda_{j_2} \quad \ldots$$

From the definition of $q(x)$, we derive a recurrence relationship for the elementary symmetrical polynomials of ω_j, $j = 0, \dots, N$ which does not require knowledge of the poles:

$$\begin{aligned} s_0 &= t_0 \quad s_1 = t_1 + iat_0 \quad s_{N+1} = iat_N - \gamma t_{N-1} \\ s_n &= t_n + iat_{n-1} - \gamma(N-n+2)t_{n-2} \quad n = 2, \dots, N. \end{aligned} \tag{B.3}$$

Using (B.2) and the residue definition, we find

$$\text{Res}(\Psi, \omega_j) = \frac{1}{i}\frac{\sum_{k=0}^{N}(-1)^k\omega_j^{N-k}}{\sum_{k=0}^{N}(-1)^k s_k(N+1-k)\omega_j^{N-k}} \quad j = 0, \dots, N. \tag{B.4}$$

Therefore, the algorithm to compute $J(t)$ in (12) can be summarized as follows.

1. Compute t_j the elementary symmetrical polynomials of $i\lambda_j$, $j = 0, \dots, N$;
2. Compute $s_0, \dots, s_{N+1}$ using (B.3);
3. Numerically find ω_j, $j = 0, \dots, N$, the roots of $q(i\omega)$;
4. Compute the residues using (B.4);
5. Evaluate the integral with (B.1).

Appendix C. Adjusted MFPT

Let T^1_{exit} be the first exit time for a certain layer and T_{final} be the final time of the simulation. Assuming that for t sufficiently large the probability density $p(t)$ of T^1_{exit} has the form $p(t) \approx a_1e^{-a_2t}$ for some positive constants a_1, a_2, then the expected first passage time conditioned on the fact that the path survives beyond T_{final} satisfies [24]

$$\mathbb{E}[T^1_{\text{exit}}|T^1_{\text{exit}} > T_{\text{final}}] = \frac{\int_{T_{\text{final}}}^\infty tp(t)dt}{\int_{T_{\text{final}}}^\infty p(t)dt} \approx \frac{\int_T^\infty ta_1e^{-a_2t}dt}{\int_T^\infty a_1e^{-a_2t}dt} = T_{\text{final}} + \frac{1}{a_2}.$$

Supplementary material

Supplementary material associated with this article can be found, in the online version, at 10.1016/j.jnnfm.2017.03.001.

References

[1] G. Massiera, K.M. Van Citters, P.L. Biancaniello, J.C. Crocker, Mechanics of single cells: rheology, time dependence, and fluctuations, Biophys. J. 93 (10) (2007) 3703–3713.

[2] J.N. Wilking, T.E. Angelini, A. Seminara, M.P. Brenner, D.A. Weitz, Biofilms as complex fluids, MRS Bull. 36 (05) (2011) 385–391, doi:10.1557/mrs.2011.71.

[3] C. Storm, J.J. Pastore, F. MacKintosh, T. Lubensky, P.A. Janmey, Nonlinear elasticity in biological gels, Nature 435 (2005).

[4] D.B. Hill, P.A. Vasquez, J.W.R. Mellnik, S.A. McKinley, A. Vose, F. Mu, A.G. Henderson, S.H. Donaldson, N.E. Alexis, R.C. Boucher, M.G. Forest, A biophysical basis for mucus solids concentration as a candidate biomarker for airways disease, PLoS ONE 9 (2) (2014) e87681, doi:10.1371/journal.pone.0087681.

[5] S.K. Lai, Y.-Y. Wang, D. Wirtz, J. Hanes, Micro-and macrorheology of mucus, Adv. Drug Deliv. Rev. 61 (2) (2009) 86–100, doi:10.1016/j.addr.2008.09.012.

[6] T.G. Mason, D.A. Weitz, Optical measurements of frequency-dependent linear viscoelastic moduli of complex fluids, Phys. Rev. Lett. 74 (7) (1995) 1250–1253.

[7] T.G. Mason, Estimating the viscoelastic moduli of complex fluids using the generalized Stokes-Einstein equation, Rheol. Acta 39 (2000) 371–378.

[8] T.M. Squires, T.G. Mason, Fluid mechanics of microrheology, Annu. Rev. Fluid Mech. 42 (2010) 413–438, doi:10.1146/annurev-fluid-121108-145608.

[9] G. Klein, Mean first-passage times of Brownian motion and related problems, Proc. R. Soc. London Series A 211 (1952) 431–443, doi:10.1098/rspa.1952.0051.

[10] C. Newman, A surface view of first-passage percolation, Proc. Int. Congress Math. 1, 2 (1995) 1017–1023.

[11] N. Georgiou, F. Rassoul-Agha, Seppäläinen, Geodesics and the competition interface for the corner growth model, Probab. Theory Relat. Fields (2016), doi:10.1007/s00440-016-0734-0.

[12] D. O'Malley, J.H. Cushman, G. Johnson, Scaling laws for fractional Brownian motion with power-law clock, J. Stat. Mech: Theory Exp. 2011 (01) (2011) L01001, doi:10.1088/1742-5468/2011/01/L01001.

[13] S.N. Majumdar, A. Rosso, A. Zoia, Hitting probability for anomalous diffusion processes, Phys. Rev. Lett. 104 (2010) 020602, doi:10.1103/PhysRevLett.104.020602.

[14] G. Rangarajan, M. Ding, First passage time distribution for anomalous diffusion, Phys. Lett. A 273 (2000) 322–330, doi:10.1088/1742-5468/2011/01/L01001.

[15] S.C. Weber, J. Theriot, A. Spakowitz, Subdiffusive motion of a polymer composed of subdiffusive monomers, Physical Review E 82 (2010) 011913, doi:10.1103/PhysRevE.82.011913.

[16] M. Magdziarz, A. Weron, K. Burnecki, Fractional Brownian motion versus the continuous-time random walk: a simple test for subdiffusive dynamics, Phys. Rev. Lett. 103 (18) (2009) 180602, doi:10.1103/PhysRevLett.103.180602.

[17] M. Lysy, N.S. Pillai, D.B. Hill, M.G. Forest, J.W.R. Mellnik, P.A. Vasquez, S.A. McKinley, Model comparison and assessment for single particle tracking in biological fluids, J. Am. Stat. Assoc. (2016).

[18] K. Xu, M. Forest, I. Klapper, On the correspondence between creeping flows of viscous and viscoelastic fluids, J. Nonnewton Fluid Mech. 145 (2–3) (2007) 150–172, doi:10.1016/j.jnnfm.2007.06.003.

[19] R. Zwanzig, Nonlinear generalized Langevin equations, J. Stat. Phys. 9 (3) (1973) 215–220.

[20] D.S. Grebenkov, V. M., Analytical solution of the generalized Langevin equation with hydrodynamic interactions: subdiffusion of heavy tracers, Phys. Rev. E 89 (2014) 012130, doi:10.1103/PhysRevE.89.012130.

[21] T. Indei, J.D. Schieber, A. Córdoba, E. Pilyugina, Treating inertia in passive microbead rheology, Phys. Rev. E 85 (021504) (2012), doi:10.1103/PhysRevE.85.021504.

[22] A. Córdoba, T. Indei, J.D. Schieber, Elimination of inertia from a generalized Langevin equation: applications to microbead rheology modeling and data analysis, J. Rheol. 56 (1) (2012) 185–212, doi:10.1122/1.3675625.

[23] S.A. McKinley, L. Yao, M.G. Forest, Transient anomalous diffusion of tracer particles in soft matter, J. Rheol. 53 (6) (2009) 1487–1506, doi:10.1122/1.3238546.

[24] S.A. McKinley, Personal communication, 2016.

[25] C. Hohenegger, On equipartation of energy and integrals of generalized Langevin equations with generalized rouse kernel, 2016. Submitted.

[26] C. Hohenegger, S.A. McKinley, Fluid-particle dynamics for passive tracers advected by a thermally fluctuating viscoelasitc medium, 2016. Submitted.

[27] R.G. Larson, Constitutive Equations for Polymer Melts and Solutions, Butterworth-Heinemann, 1988.

[28] S.C. Kou, Stochastic modeling in nanoscale biophysics: subdiffusion within proteins, Ann. Appl. Stat. 2 (2) (2008) 501–535, doi:10.1214/07-AOAS149.

[29] S. Asmussen, P.W. Glynn, Stochastic Simulation: Algorithms and Analysis, 57, Springer, 2007.

[30] H.M. Schaink, J.J.M. Slot, R.J.J. Jongschaap, J. Mellema, The rheology of systems containing rigid spheres suspended in both viscous and viscoelastic media, studied by stokesian dynamics simulations, J. Rheol. 44 (3) (2000) 473–498, doi:10.1122/1.551097.

[31] M. G'omez-Gonz'alez, D.A.J. Carlos, Two-point particle tracking microrheology of nematic complex fluids, Soft Matter 12 (2016) 5758–5779, doi:10.1039/C6SM00769D.